ACS APPLIED MATERIALS & INTERFACES

Research Article

www.acsami.org

Single-Crystalline, Ultrathin $ZnGa_2O_4$ Nanosheet Scaffolds To Promote Photocatalytic Activity in CO_2 Reduction into Methane

Qi Liu,[∥,⊥,▽] Di Wu,[○] Yong Zhou,*[,†,‡,§,∥] Haibin Su,[○] R. Wang,[§] Chunfeng Zhang,[‡,§,∥] Shicheng Yan,[∥,⊥] Min Xiao,[‡,§,∥] and Zhigang Zou*[,‡,§,∥]

[†]Key Laboratory of Modern Acoustics, MOE, Institute of Acoustics, School of Physics, [‡]National Laboratory of Solid State Microstructures, [§]School of Physics, [∥]Ecomaterials and Renewable Energy Research Center (ERERC), and [⊥]Department of Materials Science and Engineering, Nanjing University, Nanjing, Jiangsu 210093, P. R. China

[▽]School of Mechanical and Automotive Engineering, Anhui Polytechnic University, Wuhu 241000, P. R. China

[○]Division of Materials Science, Nanyang Technological University, Singapore 639798

Supporting Information

ABSTRACT: Uniform hierarchical microspheres scaffolded from ultrathin $ZnGa_2O_4$ nanosheets with over 99% exposed facets were synthesized using an easy solvothermal route with ethylenediamine (en)/H_2O binary solvents. Substitution of different chain length amines for en results in no formation of the nanosheet structures, indicating that the molecular structure of En is indispensable for the generation of two-dimensional structures. Inheriting both a high surface area of nanosheets and a high crystallinity of bulky materials allows the unique 3D hierarchical nanostructures to possess great CO_2 photocatalytic performance. The normalized time-resolved traces of photo-induced absorption recorded from the nanosheet and meso-$ZnGa_2O_4$ indicate that the photo-excited carriers can survive longer on the nanosheet, which also contributes to the high photocatalytic activity of the $ZnGa_2O_4$ nanosheets.

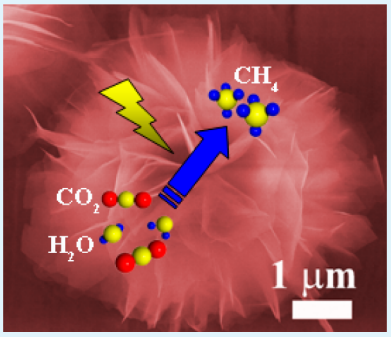

KEYWORDS: *zinc gallate, ultrathin nanosheet, microstructure, photocatalysis, CO_2 conversion*

1. INTRODUCTION

Photocatalytic conversion of CO_2 to valuable hydrocarbons using solar energy is one of the best solutions to both the global warming and the energy shortage problems. The idea of mimicking the overall natural photosynthetic cycle of the chemical conversion of CO_2 into useful fuels has been consistently gaining attention for more than 30 years.[1−4] While TiO_2-based semiconductor photocatalysts are considered the most popular for the CO_2 photoconversion,[5−8] considerable new photocatalysts have been explored to enhance the photocatalytic conversion efficiency,[9−13] and photocatalytic activities show strong dependence on the geometrical shape of the photocatalysts.[14−19] We recently synthesized single-crystalline Zn_2GeO_4 nanoribbon with exposed {010} facets and found the ultrathin nanostructure greatly promotes the photocatalytic activity of the CO_2 reduction.[14]

$ZnGa_2O_4$ has attracted considerable attention as an important member of photocatalysts, which was demonstrated to exhibit excellent performance in degradation of organic contaminants,[20−22] water splitting,[23] and reduction of CO_2.[24] We explored mesoporous $ZnGa_2O_4$ through an ion-exchange process route.[24] The as-prepared meso-$ZnGa_2O_4$ shows a high photocatalytic activity for converting CO_2 to CH_4 under light irradiation due to the strong gas adsorption and large specific surface area of the mesostructure. Besides the specific surface area, the exposed crystal facets of photocatalysts also play a critical role in determining their photocatalytic reactivity and efficiency because surface atomic arrangement and coordination changes with crystal facets. So many micro/nano-sized anatase TiO_2 crystallites with highly energetic (001) facets exposed have been successfully synthesized and do exhibit excellent photocatalytic efficiency.[25−30]

In this paper, we for the first time synthesize single-crystalline, ultrathin $ZnGa_2O_4$ nanosheets with thickness as thin as ∼6 nm (corresponding to seven repeating cell units) through a solvothermal route using ethylenediamine (en)/water binary solvent. The unique nanosheet inherits both large surface area of nanoparticles and high crystallinity of bulky materials, which allows ∼35% enhancement of photocatalytic conversion performance of CO_2 into methane, compared with the *meso*-$ZnGa_2O_4$.[24]

2. EXPERIMENTAL SECTION

2.1. Preparation of the $ZnGa_2O_4$ Samples. All the chemicals were of analytical grade and used as received without further purification. In a typical synthesis of nanosheet-based hierarchical $ZnGa_2O_4$ microsphere, 0.26 g of $Ga(NO_3)_3$ (1 mmol) and 0.11 g of $Zn(CH_3COO)_2{\cdot}2H_2O$ (0.5 mmol) were added to 15 mL of solvents which includes 10 mL of H_2O and 5 mL of ethylenediamine (en). The mixture was stirred for 40 min and then transferred to a stainless

Received: October 16, 2013
Accepted: January 29, 2014
Published: January 29, 2014

Teflon-lined autoclave of 25 mL inner volume. The solvothermal reaction was performed under an auto-generated pressure at 180 °C for 24 h in an electric oven, followed by cooling naturally to room temperature. The product was collected by centrifugation, washed thoroughly with deionized water and alcohol several times, and then dried at 60 °C for 12 h. A white $ZnGa_2O_4$ powder was finally obtained.

2.2. Characterization. The crystallographic phase of these as-prepared products was determined investigated by an X-ray diffractometer (XRD) (Rigaku Ultima III, Japan) using Cu Kα radiation (λ = 0.154178 nm) at 40 kV and 40 mA. The XRD patterns were obtained over the scanning range of 10°-80° at room temperature with a scan rate of 10° min^{-1}. The morphology of the powders was examined by field emission scanning electron microscopy (FESEM, FEI NOVA NANOSEM 230). Transmission electron microscopy (TEM) and high-resolution transmission electron microscopy (HRTEM) images were obtained on a JEOL JEM-2100 microscope with a LaB_6 filament and an accelerating voltage of 200 kV. The chemical compositions were analyzed with X-ray photoelectron spectroscopy (XPS, K-Alpha, THERMO FISHERSCIENTIFIC). The XPS spectrum was calibrated with respect to the binding energy of the adventitious C 1s peak at 284.8 eV. The UV−vis diffuse reflectance spectrum was recorded with a UV−vis spectrophotometer (UV-2550, Shimadzu) at room temperature and transformed to the absorption spectrum according to the Kubelka−Munk relationship. The specific surface area of the samples was measured by nitrogen sorption at 77 K on surface area and porosity analyzer (Micromeritics TriStar-3000 USA) and calculated by the BET method. To probe the carrier dynamics, we characterized the sample with the transient absorption spectroscopy (TAS) with nanosecond temporal resolution. An optical parametric amplifier (Opera Sola, Coherent) pumped by a femtosecond Ti:Sapphire regenerative amplifier (Libra, Coherent) was employed as the pump source. The laser beam at the wavelength of 266 nm with repetition rate of 1 kHz and pulse duration of ~90 fs was focused onto the sample spot with diameter about 500 μm. The excitation fluence was set to be ~1 mJ/cm^2. We used a cw diode laser at 488 nm to probe the dynamics of photo-excited carriers. Balance detection was used to record the signal which is further analyzed by averaging 5000 curves with a fast oscilloscope (DSO9254A, Agilent) to improve the signal to noise ratio.

2.3. Photocatalytic Conversion of CO_2. Before the photocatalytic reaction, the catalysts were degassed at 200 °C for 12 h under vacuum to remove the adsorption materials. The CO_2 photoreduction can be carried out at room temperature. Typically, 0.1 g of powdered photocatalyst was uniformly placed at the bottom of a Pyrex glass cell with an area of 4.2 cm^2. The reaction was in a gas-tight system with the volume of about 230 mL. The reaction setup was vacuum-treated several times, and then high-purity CO_2 gas was introduced into the reaction to achieve ambient pressure. A total of 0.4 mL of deionized water was injected into the system as reducer. After adsorption of CO_2 reached equilibrium in the dark, light photoirradiation was performed using an ultraviolet enhanced 300 W Xe arc lamp with an IR cut filter. A gas pump was used to accelerate gas diffusion. The concentration of product was determined using a Shimadzu GC-14C gas chromatograph (Shimadzu, Kyoto, Japan) equipped with a FID detector and Plot Q capillary column (30 m × 0.53 mm × 20 μm). Nitrogen gas was used as the carrier, and the temperature of FID was about 150 °C. The quantum yield was measured by inserting 280 nm band-pass filter in front of the reaction cell to supply the irradiant light with wavelength of 280 ± 15 nm.

3. RESULTS AND DISCUSSION

The FE-SEM images at different magnification show that the prepared $ZnGa_2O_4$ is entirely composed of quite uniform, monodisperse, spherical microstructure with diameter of 4−5 μm (Figure 1 and Supporting Information Figure S1) with volume ratio en/water (V_{en}/V_{water}) of 1:2. The close image reveals that the individual microsphere consists of hundreds of 2D ultrathin nanosheets with a length and width of several micrometres (Figure 1c), similar to peony flowers. The single

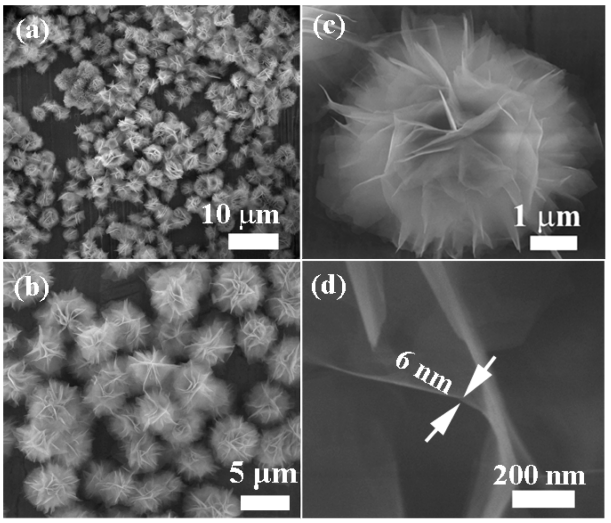

Figure 1. FE-SEM images at different magnifications of ultrathin nanosheet-scaffolded microspheres prepared with V_{en}/V_{water} ratio 1:2.

nanosheet is as thin as about ~6 nm measured from the vertically standing one (Figure 1d). Noticeably, unlike its sheet-like analogue such as graphene,[31−33] the present 3D scaffolding allows the $ZnGa_2O_4$ ultrathin nanosheets to be spatially stable against stacking aggregation to preserve the active sites for photocatalytic reduction of CO_2 below.

The TEM images further reveal that the $ZnGa_2O_4$ nanosheet-scaffolded microstructure was built of the number of sheet components (Figure 2). The light contrast of the

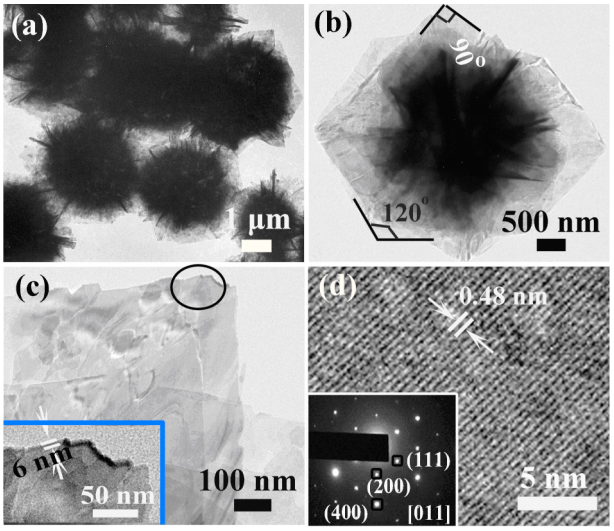

Figure 2. (a and b) TEM images of ultrathin nanosheet-scaffolded $ZnGa_2O_4$ microspheres; (c) TEM image of single nanosheets. The inset shows the high magnification taken from the top-right region circled in (c). (d) HRTEM images of nanosheets. The inset shows the SAED pattern indexed to the $[01\bar{1}]$ zone. The image show lattice fringes with a spacing of 0.48 nm.

nanosheet indicates extremely thin thickness. The nanosheets are generally shaped as square and hexagonal outline with average length of ~3 μm. The thickness of the nanosheet was measured about ~6 nm from the edge of the curved nanosheets approximately perpendicular to the support film (inset of Figure 2c), consistent with SEM observation. The high-

dx.doi.org/10.1021/am404572g | ACS Appl. Mater. Interfaces 2014, 6, 2356−2361

resolution TEM (HRTEM) image demonstrates the interplanar *d*-spacing of lattice fringes of 0.48 nm and corresponds to (111) lattice planes of the cubic $ZnGa_2O_4$. The selected area electron diffraction (SAED) pattern (the inset of Figure 2d) along [01$\bar{1}$] zone exhibits clear diffraction spots with good alignment, indicative of the well-defined single crystal structure of the nanosheet.

The percentages of {110} facets were estimated on the basis of the total surface area of nanosheet and TEM results. Assuming that the nanosheets of $ZnGa_2O_4$ microcrystals are square, the percentages of {110} facets are approximately calculated as follows:[34,35]

$$\{110\}\% = \frac{\text{Surface area of } \{110\} \text{ planes}}{\text{The total surface area of nanosheet}} \times 100\%$$
$$= \frac{2 \times 3 \times 3}{4 \times 3 \times 0.007 + 2 \times 3 \times 3} \times 100\%$$
$$\approx 99.6\%$$

If the nanosheets of $ZnGa_2O_4$ microcrystals are all hexagonal, the percentages of {110} facets are approximately calculated as follows:

$$\{110\}\% = \frac{\text{Surface area of } \{110\} \text{ planes}}{\text{The total surface area of nanosheet}} \times 100\%$$
$$= \frac{2 \times \frac{3\sqrt{3}}{2} \times 3 \times 3}{6 \times 3 \times 0.006 + 2 \times \frac{3\sqrt{3}}{2} \times 3 \times 3} \times 100\%$$
$$\approx 99.8\%$$

Thus, the nanosheet can be determined with the dominant over 99.6% exposed facets of {110} with seven repeating cell units along the thickness direction, i.e., 7 × 0.8335 nm = 5.8345 nm (Supporting Information Figure S2). The formation of the nanosheet is believed to originate from the higher growth rate of {110} than {100} and {111} mediated with en through a solvent-coordination molecular-template mechanism,[36−39] which is similar to our previously reported results over Zn_2GeO_4 nanoribbons.[14]

The X-ray diffraction (XRD) pattern show that all the diffraction peaks of the $ZnGa_2O_4$ nanosheet could be readily indexed to the cubic $ZnGa_2O_4$ (JCPDS card No. 38-1240; space group *Fd*3*m* (No. 227)) with lattice constants of $a = b = c = 8.335$ Å, $\alpha = \beta = \gamma = 90°$ (Supporting Information Figure S3). No diffraction peaks from impurities and/or other phases can be detected. The broadening of the diffraction peaks indicates small size in at least one dimension, consistent with observation of both the FE-SEM and TEM images. The significantly enhanced diffraction intensity ratio of (220) to (111) and (400) relative to the standard diffraction pattern implies that the nanosheet possesses a preferred growth orientation along {110} planes, also well in agreement with the TEM observation. The narrow-scan XPS spectrum proves the presence of Zn, Ga, and O (Supporting Information Figure S4).

To understand the formation mechanism of such a nanosheet-scaffolded $ZnGa_2O_4$ microstructure, different experimental conditions were investigated. Use of pure water as the solvent enables us to obtain monodisperse GaOOH nanorods consisting of stacking nanosheets with a diameter of around 100 nm and a length of 500 nm (Figures 3a and 4a). The large $ZnGa_2O_4$ nanosheet-based microcrystals began to appear with addition of en to the reaction solution at V_{en}/V_{water} of 1:4

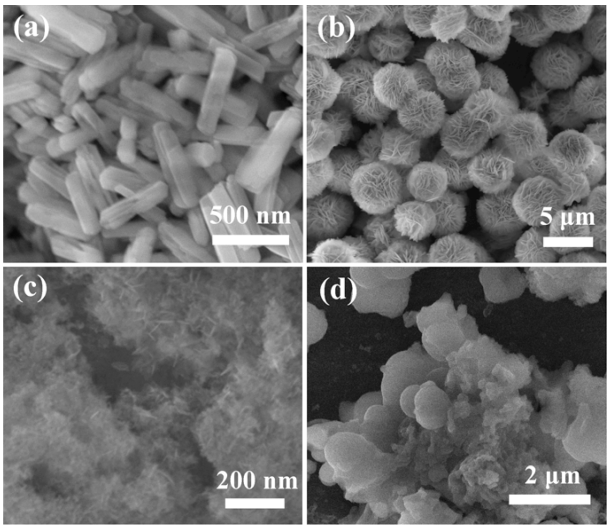

Figure 3. FE-SEM images of the products prepared with different solvents: (a) pure water as solvent; (b) V_{en}/V_{water} volume ratio of 1:4; (c) V_{en}/V_{water} volume ratio of 1:1; (d) pure En as solvent.

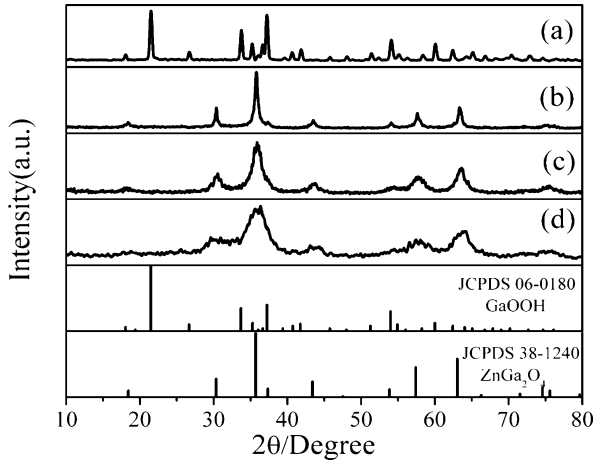

Figure 4. XRD patters of the products prepared with different solvents: (a) pure water as solvent; (b) V_{en}/V_{water} volume ratio of 1:4; (c) V_{en}/V_{water} volume ratio of 1:1; (d) pure En as solvent.

(Figures 3b and 4b). Increasing the V_{en}/V_{water} ratio from 1:4 to 1:2, well-defined $ZnGa_2O_4$ nanosheet-based microstructure can be obtained, as discussed above. When equal amounts of en and water were used at V_{en}/V_{water} of 1:1, tiny and aggregating $ZnGa_2O_4$ nanoplates were produced (Figures 3c and 4c). Employment of pure en as a single solvent produced irregular $ZnGa_2O_4$ particles (Figures 3d and 4d). As a result, both en and H_2O solvents play a synergistic effect on generation of the ultrathin $ZnGa_2O_4$ nanosheets scaffolding into the spherical microstructure. Substitution of different chain length amines (e.g., methylamine, diethylenetriamine, or oleylamine) for en results in no formation of the nanosheet structures (Supporting Information Figure S5) indicating that the molecular structure of en is indispensable for a generation of two dimensional structures.

We perform CO_2 and gaseous H_2O photocatalysis in a gas−solid system over the $ZnGa_2O_4$ nanosheet scaffolds. The photogenerated holes in the valence band oxidize water to generate hydrogen ions via the reaction of $H_2O \rightarrow {}^1/_2O_2 + 2H^+ + 2e^-$ (E°_{redox} = 0.82 V vs NHE), and the photogenerated

electrons in the conduction band reduce CO_2 to CH_4 via the reaction of $CO_2 + 8e^- + 8H^+ \rightarrow CH_4 + 2H_2O$ ($E^\circ_{redox} = -0.24$ V vs NHE). The band gap of the $ZnGa_2O_4$ nanosheet is determined based on the UV–vis absorption spectrum to be around 4.5 eV (Figure 5). The position of corresponding

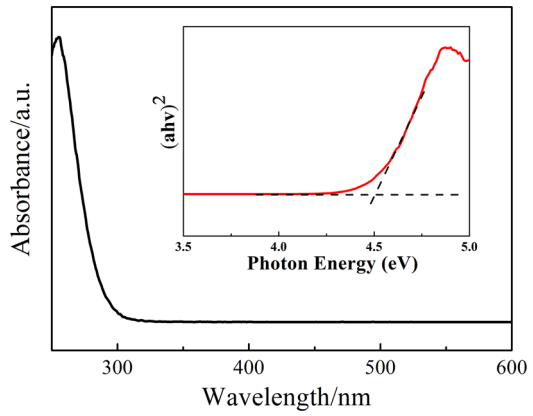

Figure 5. UV–vis adsorption spectrum of the ultrathin $ZnGa_2O_4$ nanosheet–scaffold microstructure.

conduction band and valence band could be determined by the following equation: $E_{CB} = X - E_c - 0.5E_g$, where E_c is the energy of free electrons on the hydrogen scale (4.5 eV), X is the electronegativity of the semiconductor, and E_g is band gap energy of the semiconductor. The edge of the valence band (E_{VB}) of the $ZnGa_2O_4$ nanosheet is determined to be 3.18 V (vs NHE), more positive than that of E° (H_2O/H^+) (0.82 V vs NHE), and the edge of the conduction band is estimated to be −1.32 V (vs NHE) and is more negative than that of E° (CO_2/CH_4) (−0.24 V vs NHE). It indicates that the photogenerated electrons and holes on the irradiated $ZnGa_2O_4$ nanosheet can react with adsorbed CO_2 and H_2O to produce CH_4. Figure 6 shows the photocatalytic reactivity of CO_2 reduction over

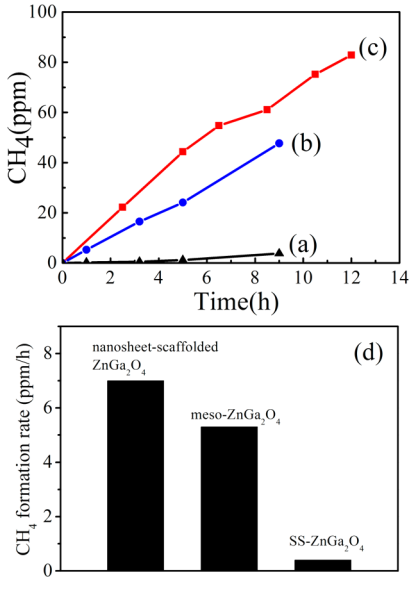

Figure 6. CH_4 generation over various $ZnGa_2O_4$ samples as a function of irradiation time: (a) SS-$ZnGa_2O_4$, (b) meso-$ZnGa_2O_4$, and (c) nanosheet-scaffolded microspheres $ZnGa_2O_4$; (d) comparison of the average 9-hour initial CH_4 formation rates.

$ZnGa_2O_4$ nanosheet along with bulky $ZnGa_2O_4$ obtained by the solid state (SS) reaction of ZnO and Ga_2O_3 at 1100 °C for 16 h, and the mesoporous $ZnGa_2O_4$ (the corresponding TEM image was shown in Supporting Information Figure S6) as compared under light illumination. The gross yield in the CH_4 of the ultrathin nanosheet increased with the photocatalytic time, and a total yield of CH_4 obtained in the experiment after 12 h of continuous irradiation is 83 ppm, corresponding to approximate 6.9 ppm/h of the CH_4 formation rate. To rule out the possibilities of residual en as carbon sources for CH_4 during photocatalytic reaction, the $ZnGa_2O_4$ nanosheets were illuminated with N_2 as the carrier gas without input of CO_2. Neither CH_4 nor other carbon compounds were detected, indicating that the generated CH_4 indeed originates from photoreduction of CO_2. CO_2 reduction experiment performed in the dark or in the absence of the photocatalyst showed no appearance of CH_4, further proving that the CO_2 reduction reaction is driven by light with the photocatalysts. The nanosheet shows obviously higher activity than SS-$ZnGa_2O_4$ (CH_4: trace), mainly ascribed to ~11 time-high surface area (S_{BET}: 55.5 $m^2\ g^{-1}$ for $ZnGa_2O_4$ nanosheets and 4.6 $m^2\ g^{-1}$ for SS-$ZnGa_2O_4$). The nanosheet scaffold also exhibits ~35% enhanced conversion rate compared to that of the *meso*-$ZnGa_2O_4$, although its BET surface area is only half that of *meso*-$ZnGa_2O_4$ (S_{BET}: 110.4 $m^2\ g^{-1}$ for *meso*-$ZnGa_2O_4$).[24] The unusual high photocatalytic activity of the ultrathin nanosheet compared with *meso*-$ZnGa_2O_4$ and bulky materials can be derived from the following five reasons: (1) The thickness dimension down to several nanometer scale with regard to the nanosheet offers a high specific surface area. (2) Ultrathin geometry of the nanogeometry allows charge carriers quickly move from the interior to the surface to participate in the photoreduction reaction, in contrast with the bulky materials. (3) The superb crystal quality of the nanosheet excludes the possibility of any grain boundaries and/or other interfaces, which usually act as recombination sites in *meso*-$ZnGa_2O_4$. This should favor improved separation of photogenerated electron and hole, lower electron-hole recombination rate, and elongate the lifetime of the carriers. To probe the carrier dynamics, we characterized the sample with the transient absorption spectroscopy with nanosecond temporal resolution[40] and investigated the photoluminescence decay profiles of the nanosheet and *meso*-$ZnGa_2O_4$ powders (Figure 7). As particle sizes in the case of both powders are very small, less than 10 nm, it can be considered that the carrier lifetime of these small

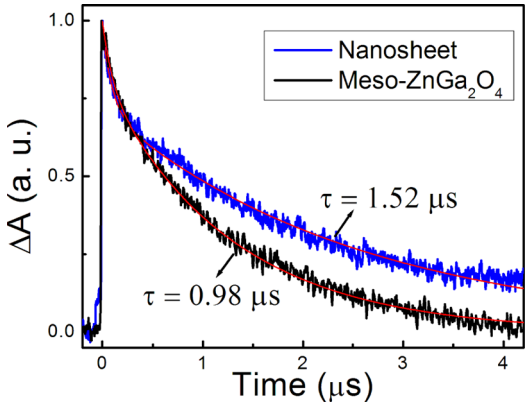

Figure 7. The normalized time-resolved traces of photo-induced absorption recorded from the nanosheet and meso-$ZnGa_2O_4$.

dx.doi.org/10.1021/am404572g | ACS Appl. Mater. Interfaces 2014, 6, 2356–2361

particles is determined by the recombination process on the surface rather than by the migration of carriers to the surface.[41] The observed slower decay profile of the nanosheet indicates that the photo-excited carriers can survive longer on the nanosheet surface. (4) Large ratio of the lateral dimension to thickness of the nanosheet provides a sufficiently spacious transport channel for charge separation. (5) The 3D hierarchical architectures increases light scattering to be in favor of enhancing the light absorption.

The quantum yield was calculated according to the below equation:[42]

$$E_Q = [N(CH_4) \times 8]/N(\text{Photons}) \times 100\%$$

in which $N(CH_4)$ and $N(\text{Photons})$ signify the molecular number of generated CH_4 in unit time and the number of incident photons in unit time, respectively. The apparent quantum yield of CH_4 evolution of $ZnGa_2O_4$ nanosheets at wavelength of 280 ± 15 nm was measured to be 0.035%. Compared with photocatalytic water splitting, the quantum yield is still low. The photo-conversion rate of the CO_2 may be further enhanced through loading some cocatalysts to improve the separation of the photogenerated electron−hole pairs, as demonstrated in photocatalytic water splitting.

4. CONCLUSION

In summary, uniform hierarchical microspheres scaffolded from ultrathin $ZnGa_2O_4$ nanosheets with over 99.6% exposed {110} facets have been synthesized through a solvothermal route with en/H_2O binary solvents. Inheriting both high surface area of nanoparticles and high crystallinity of bulky materials allows the unique 3D hierarchical nanostructures to possess great CO_2 photocatalytic performance.

■ ASSOCIATED CONTENT

Supporting Information

Experimental details of mesoporous $ZnGa_2O_4$ and additional SEM, XRD, XPS, and TEM results of the prepared materials. This material is free of charge via the Internet at http://pubs.acs.org.

■ AUTHOR INFORMATION

Corresponding Authors

*(Y.Z.) E-mail: zhouyong1999@nju.edu.cn. Tel: +86 25 8362 1372.

*(Z.Z.) E-mail: zgzou@nju.edu.cn. Tel: +86 25 8362 1372.

Notes

The authors declare no competing financial interest.

■ ACKNOWLEDGMENTS

This work was supported by 973 Programs (No. 2011CB933303, 2013CB632404), NSFC (No. 51302001 and 20971048), Anhui Province College Excellent Young Talents Fund (No. 2013SQRL036ZD), Natural Science Fund of Jiangsu Provincial (No. BK2012015), Sony Corporation, and Fundamental Research Funds for the Central Universities (No. 1113020401, 1115020405, and 1116020406).

■ REFERENCES

(1) Roy, S. C.; Varghese, O. K.; Paulose, M.; Grimes, C. A. *ACS Nano* **2010**, *4*, 1259.

(2) Baum, M. M.; Hoffmann, M. R.; Moss, J. A. *Dalton Trans.* **2011**, *40*, 5151.

(3) Tu, W. G.; Zhou, Y.; Zou, Z. G. *Adv. Funct. Mater.* **2013**, *23*, 4996.

(4) Inoue, T.; Fujishima, A.; Konishi, S.; Honda, K. *Nature* **1979**, *277*, 637.

(5) Izumi, Y. *Coord. Chem. Rev.* **2013**, *257*, 171.

(6) Habisreutinger, S. N.; Schmidt-Mende, L.; Stolarczyk, J. K. *Angew. Chem., Int. Ed.* **2013**, *52*, 7372.

(7) Mori, K.; Yamashita, H.; Anpo, M. *RSC Adv.* **2012**, *2*, 3165.

(8) Wang, W. N.; An, W. J.; Ramalingam, B.; Mukherjee, S.; Niedzwiedzki, D. M.; Gangopadhyay, S.; Biswas, P. *J. Am. Chem. Soc.* **2012**, *134*, 11276.

(9) Xi, G.; Ouyang, S.; Li, P.; Ye, J.; Ma, Q.; Su, N.; Bai, H.; Wang, C. *Angew. Chem., Int. Ed.* **2012**, *51*, 2395.

(10) In, S.-I.; Vaughn, D. D.; Schaak, R. E. *Angew. Chem., Int. Ed.* **2012**, *51*, 3915.

(11) Fu, Y.; Sun, D.; Chen, Y.; Huang, R.; Ding, Z.; Fu, X.; Li, Z. *Angew. Chem., Int. Ed.* **2012**, *51*, 1.

(12) Iizuka, K.; Wato, T.; Miseki, Y.; Saito, K.; Kudo, A. *J. Am. Chem. Soc.* **2011**, *133*, 20863.

(13) Sun, H.; Wang, S. *Energy Fuels* **2013**, *28*, 22.

(14) Liu, Q.; Zhou, Y.; Kou, J.; Chen, X.; Tian, Z.; Gao, J.; Yan, S.; Zou, Z. *J. Am. Chem. Soc.* **2010**, *132*, 14385.

(15) Tu, W. G.; Zhou, Y.; Liu, Q.; Tian, Z. P.; Gao, J.; Chen, X. Y.; Zhang, H. T.; Liu, J. G.; Zou, Z. G. *Adv. Funct. Mater.* **2012**, *22*, 1215.

(16) Chen, X. Y.; Zhou, Y.; Liu, Q.; Li, Z. D.; Liu, J. G.; Zou, Z. G. *ACS Appl. Mater. Interfaces* **2012**, *4*, 3372.

(17) Li, Z. D.; Zhou, Y.; Zhang, J. Y.; Tu, W. G.; Liu, Q.; Yu, T.; Zou, Z. G. *Cryst. Growth Des.* **2012**, *12*, 1476.

(18) Zhou, Y.; Tian, Z. P.; Zhao, Z. Y.; Liu, Q.; Kou, J. H.; Chen, X. Y.; Gao, J.; Yan, S. C.; Zou, Z. G. *ACS Appl. Mater. Interfaces* **2011**, *3*, 3594.

(19) Yan, S. C.; Wang, J. J.; Gao, H. L.; Wang, N. Y.; Yu, H.; Li, Z. S.; Zhou, Y.; Zou, Z. G. *Adv. Funct. Mater.* **2013**, *23*, 758.

(20) Zhang, W. W.; Zhang, J. Y.; Lan, X. A.; Chen, Z. Y.; Wang, T. M. *Catal. Commun.* **2010**, *11*, 1104.

(21) Zhang, X. N.; Huang, J. H.; Ding, K. N.; Hou, Y. D.; Wang, X. C.; Fu, X. Z. *Environ. Sci. Technol.* **2009**, *43*, 5947.

(22) Zhang, W. W.; Zhang, J. Y.; Chen, Z. Y.; Wang, T. M. *Catal. Commun.* **2009**, *10*, 1781.

(23) Kumagai, N.; Ni, L.; Irie, H. *Chem. Commun.* **2011**, *47*, 1884.

(24) Yan, S. C.; Ouyang, S. X.; Gao, J.; Yang, M.; Feng, J. Y.; Fan, X. X.; Wan, L. J.; Li, Z. S.; Ye, J. H.; Zhou, Y.; Zou, Z. G. *Angew. Chem., Int. Ed.* **2010**, *49*, 6400.

(25) Wu, B. H.; Guo, C. Y.; Zheng, N. F.; Xie, Z. X.; Stucky, G. D. *J. Am. Chem. Soc.* **2008**, *130*, 17563.

(26) Jiang, H. B.; Cuan, Q. A.; Wen, C. Z.; Xing, J.; Wu, D.; Gong, X. Q.; Li, C. Z.; Yang, H. G. *Angew. Chem., Int. Ed.* **2011**, *50*, 3764.

(27) Chen, J. S.; Tan, Y. L.; Li, C. M.; Cheah, Y. L.; Luan, D. Y.; Madhavi, S.; Boey, F. Y. C.; Archer, L. A.; Lou, X. W. *J. Am. Chem. Soc.* **2010**, *132*, 6124.

(28) Yang, H. G.; Liu, G.; Qiao, S. Z.; Sun, C. H.; Jin, Y. G.; Smith, S. C.; Zou, J.; Cheng, H. M.; Lu, G. Q. *J. Am. Chem. Soc.* **2009**, *131*, 4078.

(29) Liu, G.; Yang, H. G.; Wang, X. W.; Cheng, L. N.; Pan, J.; Lu, G. Q.; Cheng, H. M. *J. Am. Chem. Soc.* **2009**, *131*, 12868.

(30) Han, X. G.; Kuang, Q.; Jin, M. S.; Xie, Z. X.; Zheng, L. S. *J. Am. Chem. Soc.* **2009**, *131*, 3152.

(31) Chen, J. S.; Tan, Y. L.; Li, C. M.; Cheah, Y. L.; Luan, D. Y.; Madhavi, S.; Boey, F. Y. C.; Archer, L. A.; Lou, X. W. *J. Am. Chem. Soc.* **2010**, *132*, 6124.

(32) Yang, W. G.; Li, J. M.; Wang, Y. L.; Zhu, F.; Shi, W. M.; Wan, F. R.; Xu, D. S. *Chem. Commun.* **2011**, *47*, 1809.

(33) Shi, J.; Ye, J.; Li, Q.; Zhou, Z.; Tong, H.; Xi, G.; Guo, L. *Chem.—Eur. J.* **2012**, *18*, 3157.

(34) Sun, L.; Qin, Y.; Cao, Q.; Hu, B.; Huang, Z.; Ye, L.; Tang, X. *Chem. Commun.* **2011**, *47*, 12628.

(35) Liu, S. S.; Yang, D. P.; Ma, D. K.; Wang, S.; Tang, T. D.; Huang, S. M. *Chem. Commun.* **2011**, *47*, 8013.

(36) Wang, Z. L. *J. Phys. Chem. B* **2000**, *104*, 1153.

(37) Li, Y. D.; Liao, H. W.; Ding, Y.; Fan, Y.; Zhang, Y.; Qian, Y. T. *Inorg. Chem.* **1999**, *38*, 1382.
(38) Yao, W. T.; Yu, S. H. *Adv. Funct. Mater.* **2008**, *18*, 3357.
(39) Song, R. Q.; Xu, A. W.; Yu, S. H. *J. Am. Chem. Soc.* **2007**, *129*, 4152.
(40) Cowan, A. J.; Barnett, C. J.; Pendlebury, S. R.; Barroso, M.; Sivula, K.; Graetzel, M.; Durrant, J. R.; Klug, D. R. *J. Am. Chem. Soc.* **2011**, *133*, 10134.
(41) Rothenberger, G.; Moser, J.; Gratzel, M.; Serpone, N.; Sharma, D. K. *J. Am. Chem. Soc.* **1985**, *107*, 8054.
(42) Liu, Q.; Zhou, Y.; Tian, Z.; Chen, X.; Gao, J.; Zou, Z. *J. Mater. Chem.* **2012**, *22*, 2033.